Original Article

Developing of risk models for small solid and subsolid pulmonary nodules based on clinical and quantitative radiomics features

Rui Zhang[1], Huaiqiang Sun[2], Bojiang Chen[1], Renjie Xu[3], Weimin Li[1]

[1]Department of Pulmonary and Critical Care Medicine, West China Hospital of Sichuan University, Chengdu, China; [2]Huaxi MR Research Center, Department of Radiology, West China Hospital of Sichuan University, Chengdu, China; [3]Department of Research and Development, Shanghai United Imaging Intelligence Co., Ltd., Shanghai, China

Contributions: (I) Conception and design: W Li, R Zhang; (II) Administrative support: W Li; (III) Provision of study materials or patients: R Zhang, B Chen; (IV) Collection and assembly of data: R Zhang, H Sun; (V) Data analysis and interpretation: R Zhang, H Sun, R Xu; (VI) Manuscript writing: All authors; (VII) Final approval of manuscript: All authors.

Correspondence to: Weimin Li. Department of Respiratory and Critical Care Medicine, West China Hospital, Sichuan University, #37 GuoXue Alley, Chengdu 610041, China. Email: weimi003@yahoo.com.

Background: Accurate evaluation of pulmonary nodule malignancy is important for lung cancer management. This current study aimed to develop risk models for small solid and subsolid pulmonary nodules based on clinical and quantitative radiomics features.

Methods: This study enrolled 5–20 mm pulmonary nodules detected on thoracic high-resolution computed tomography (HRCT), which were all confirmed pathologically. There were 548 solid nodules (242 malignant *vs.* 306 benign) and 623 subsolid nodules (SSNs 519 malignant *vs.* 104 benign). Relevant clinical characteristics were recorded. The CT image prior to the initial treatment was chosen for manual segmentation of the targeted nodule using the ITK-SNAP software. Subsequently, the marked image was processed to quantitatively extract 1218 radiomics features using PyRadiomics. We performed five-fold cross-validation to select potential predictors from clinical and radiomics features using the LASSO method and to evaluate the performance of the established models. In total, four types of models were tried: random forest, XGBOOST, SVM, and logistic models. The established models were compared with the Mayo model.

Results: Lung cancer risk models were developed among four nodule groups: all nodules (410 benign *vs.* 761 malignant; 1:1.86), nodules ≤10 mm (185 benign *vs.* 224 malignant; 1:1.21), solid nodules (306 benign *vs.* 242 malignant; 1.26:1), and SSNs (104 benign *vs.* 104 malignant; 1:1 matched). Significant clinical and radiomics predictors were selected for each group. The accuracy, area under the ROC curve, sensitivity, and specificity of the best model on validation dataset was 0.86, 0.91, 0.93, 0.73 for all nodules (XGBOOST), 0.82, 0.90, 0.86, 0.76 for nodules ≤10 mm (XGBOOST), 0.80, 0.89, 0.78, 0.82 for solid nodules (XGBOOST) and 0.70, 0.73, 0.73, 0.67 for SSNs (Random Forest). Except for the SSN models, the established clinical-radiomics models were superior to the Mayo model.

Conclusions: Predictive models based on both clinical and radiomics features can be used to assess the malignancy of small solid and subsolid pulmonary nodules, even for nodules that are 10 mm or smaller.

Keywords: Radiomics; solid nodules; subsolid nodules; lung cancer; risk model

Submitted Jan 12, 2021. Accepted for publication Jun 04, 2021.
doi: 10.21037/jtd-21-80
View this article at: https://dx.doi.org/10.21037/jtd-21-80

Introduction

The International Agency for Research on Cancer reported that lung cancer was the most commonly diagnosed cancer (11.6% of the total cases) and the leading cause of cancer death (18.4% of the total cancer deaths) for both sexes in 2018 (1). Hence, efficient strategies are necessary to manage the disease. Early stage lung cancer usually presents as a solitary pulmonary nodule on thoracic computed tomography (CT), namely, a rounded lesion measuring less than 30 mm in diameter, which is completely surrounded by pulmonary parenchyma without other pulmonary abnormalities (2). According to its texture, nodules can be classified into subsolid nodules (SSNs) or solid nodules (3). Accurate characterization of pulmonary nodules, especially regarding their likelihood of malignancy, can be very important in lung cancer management.

Traditionally, thoracic radiologists and clinicians rely largely on qualitative morphological features such as texture, spiculation, lobulation, calcification, pattern of enhancement, presence of blood vessels, impact on adjacent structures, and so on, to evaluate the nature of pulmonary nodules (4). For example, a smoothly marginated solid nodule with internal fat and calcification can be a hamartoma, and a solid triangular subpleural nodule with a linear extension to the pleural surface is typical of an intrapulmonary lymph node, where no further CT follow-up is recommended (3). In addition, nodule size, nodule type, spiculation, upper lobe location, ^{18}F-fluorodeoxyglucose uptake, and volume doubling time (VDT) could be independent predictors of malignancy (5-8). However, morphological features can sometimes overlap between benign and malignant nodules, so the morphological features are not sufficient to assess the likelihood of malignancy (9). In addition, inter- and intraobserver agreement in evaluating nodule features was found to be highly variable (10). Moreover, nodules less than 10 mm in size, which account for approximately 80% of all non-calcified nodules, are less amenable than larger nodules when it comes to characterization (11).

At present, a rapidly evolving field called radiomics, which enables digital decoding of images into quantitative features, including descriptors of size, shape, and textural features, has shown promise in characterizing lung cancers (12). For example, previous radiomics studies were successfully performed to identify epidermal growth factor receptor mutations, classify tumor histologic subtype, and predict tumor invasiveness as well as lymph node and distant metastasis (13). Therefore, the current study aimed to develop risk models for small solid and subsolid pulmonary nodules (5–20 mm) based on clinical and quantitative radiomics features.

We present the following article in accordance with the TRIPOD reporting checklist (available at https://dx.doi.org/10.21037/jtd-21-80).

Methods

Patient enrollment

Data were retrospectively collected from the West China Hospital of Sichuan University between January 2010 and July 2017. Patients were enrolled if there was an untreated, pathologically confirmed, 5–20 mm, dominant, noncalcified SSN, or solid nodule on thoracic high-resolution CT (HRCT). The study included incidental pulmonary nodules and annually screen detected nodules. Patients were excluded if (I) multiple pulmonary nodules were observed, where nodules distributed diffusely or multiple nodules were confirmed to be tumors or if there were several problematic nodules; (II) pleural effusion, atelectasis, or lymph node enlargement was observed; and (III) the pathological diagnosis was not clear or it was a metastatic tumor. Pathological diagnoses of all nodules were based on sputum cytology or pathologic examination of lung tissues obtained from bronchoscopy, CT-guided percutaneous lung biopsy, or thoracic surgery. In total, 1,855 patients with 5–20 mm pathologically confirmed nodules were found, and 1,171 patients were enrolled for further analysis, as the segmentation of two patients failed and 682 patients did not have HRCT.

Collection of clinical variables

Clinical characteristics were recorded, including age, sex, smoking status, history of malignancy, and family history of lung cancer (demographic); diameter, location, shape, spiculation, lobulation (radiologic), red blood cells, white blood cells, blood platelets, neutrophil to lymphocyte ratio (NLR), prothrombin time, activated partial thromboplastin time (APTT), carcinoembryonic antigen (CEA), cytokeratin 19 fragment (CYFRA21-1) and neuron specific enolase (NSE, laboratory). This study was approved by the institutional review board of the West China Hospital of Sichuan University, and the requirement to obtain informed consent was waived as the privacy and identity information

of the subjects were guaranteed. There were some missing data regarding CEA, CYFRA21-1, and NSE tests, which were populated by the median value. The data were not available as some of the patients did not undergo testing.

CT image acquisition

The CT image chosen was the one prior to the initial treatment. All images were acquired using several models of multi-row spiral CT scans from GE, Siemens or Philips scanners. Most CT scans were obtained between 100 and 120 kV. The pixel size was 0.7 to 0.9 mm, and the axial slice thickness was less than 1.25 mm, with 1 mm being the most common. Reconstruction was performed using a standard convolution kernel. Some patients underwent non-contrast CT examination while others underwent contrast-enhanced CT. All images were analyzed in both lung (width, 1,500 HU; level, –700 HU) and mediastinal (width =350 HU; level =40 HU) settings. During patient selection and radiologic feature evaluation, two specialists who were blinded to the pathological results of lesions evaluated all CT scans and resolved discrepancies by consensus.

Nodule segmentation and feature extraction

The target nodules were manually segmented in 3D using the ITK-SNAP software by one clinician in pulmonary and critical care medicine, with four years of experience in pulmonary nodule evaluation (14). The author was also blinded to the pathological results of all the lesions. Radiomics feature extraction was performed using the open-source platform Pyradiomics (version 2.0.0), which enables quantitative features to be extracted from HRCT images (12). Extracted from Pyradiomics were 14 shape features, 18 first-order features, 22 gray-level co-occurrence matrix (GLCM) features, 16 gray-level size zone matrix (GLSZM) features, 16 gray-level run length matrix (GLRLM) features, and 14 gray-level dependence matrix (GLDM) features. Except for shape features, other features were also calculated from the filtered images (LoG with five sigma levels and wavelet with eight derived images). In total, 1,218 radiomics features [14 shape features + 86 other features × (1 original image + 13 filtered images)] were generated for each nodule. A detailed list of the extracted features is provided in Table S1.

Model establishment

All risk models were established in two steps: feature selection and model development. The least absolute shrinkage and selection operator (LASSO) method was applied to select the most significant predictors from clinical and radiomics features simultaneously. Then, four types of models were tried for each nodule group based on selected features, including random forest, XGBOOST, SVM, and logistic model. We normalized the data using the Z-score to allow all the coefficients to be based on the same scale and performed five-fold cross-validation during both steps.

Performance of models

The model performance was evaluated using metrics such as the area under the ROC curve (AUC), accuracy, F1 score, recall, precision, sensitivity, and specificity. The performance of the models was compared with the predictive ability of the Mayo model (5). All cases in each group were utilized to validate the Mayo model, and the corresponding AUC, accuracy, sensitivity, and specificity were calculated.

Statistical analysis

The numerical data were presented as mean ± standard deviation and compared using Student's t-test, while categorical data were described as percentages and compared using the chi-square test. All statistical tests were two-sided, and differences were considered statistically significant at $P<0.05$. All statistical analyses were performed with R version 3.6, and all models were established using Python 3.7.

Ethical statement

The study was conducted in accordance with the Declaration of Helsinki (as revised in 2013). The study was approved by the institutional review board of the West China Hospital of Sichuan University (No.59). Informed consent was waived as this was a retrospective study and the privacy and identity information of the subjects were guaranteed.

Results

Patient enrollment and pathology of nodules

Figure 1 presents the flowchart of the study process. A total of 1,171 patients who met the inclusion criteria

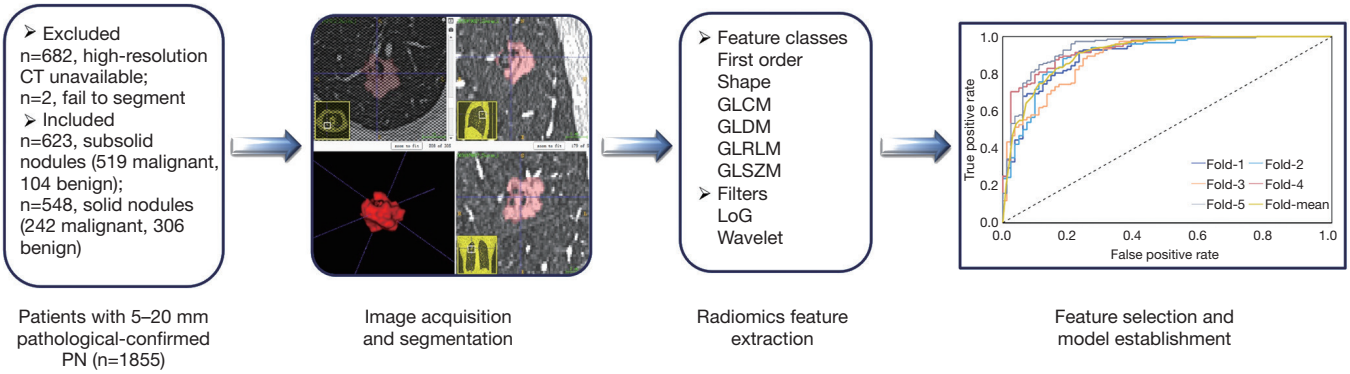

Figure 1 The workflow of the current study. PN, pulmonary nodule.

were enrolled, including 548 patients with solid nodules (malignant, 242; benign, 306) and 623 patients with SSNs (malignant, 519; benign, 104). All nodules were confirmed pathologically. The benign group included inflammatory nodules (62.20%), benign tumors (20.00%), and other lesions (17.80%). Malignant nodules were mainly adenocarcinomas (97.37%), while 1.97% were squamous carcinomas and 0.66% were other types (Table S2).

Patient clinical characteristics

The clinical characteristics of the patients are summarized in *Table 1*. In patients with solid nodules, the benign and malignant groups exhibited some differences in age, history of malignancy, diameter, shape, spiculation, lobulation, white blood cell count, NLR, APTT, and CEA (P<0.05). As for SSNs, there was no difference in the proportion of history of malignancy, white blood cell count, NLR, and CEA between the benign and malignant groups. However, significant differences in age, diameter, location, shape, spiculation, lobulation, APTT, CYFRA21-1, and NSE were observed between the malignant and benign groups (P<0.05). Details of missing data for CEA, CYFRA21-1, and NSE are described in Table S3.

Model establishment and selected radiomics features

We developed lung cancer risk models among four nodule groups: all nodules (n=1,171), nodules ≤10 mm (n=409), solid nodules (n=548), and SSNs (n=208). To avoid overfitting of models in the SSN group, only 104 malignant SSNs were included, which were 1:1 matched with benign SSNs.

Table S4 summarizes the selected features from LASSO analysis in detail for all nodules (α=0.00955, n=74 features), nodules ≤10 mm (α=0.0152, n=67 features), solid nodules (α=0.0152, n=51 features), and SSNs (α=0.12328, n=3 features). *Figure 2* describes the top ten features sorted by the absolute value of coefficients and the rad-score distribution based on selected features for all nodules (*Figure 2A*,*B*,*C*) and nodules ≤10 mm (*Figure 2D*,*E*,*F*). In addition, the top ten features for solid nodules, all three features for SSNs, and the corresponding rad-score distribution for solid nodules (*Figure 3A*,*B*,*C*) and SSNs (*Figure 3D*,*E*,*F*) are shown in *Figure 3*. There was a higher proportion of radiomics features selected for nodules ≤10 mm (83.6% of 67 features and 80% of the top ten features).

Performance of risk models

We performed five-fold cross-validation to evaluate the predictive performance of the lung cancer risk models. According to the accuracy of the training dataset, the top three models for each nodule group were recorded. For all nodules (410 benign *vs.* 761 malignant; 1:1.86), nodules ≤10 mm (185 benign *vs.* 224 malignant; 1:1.21), and solid nodules (306 benign *vs.* 242 malignant; 1.26:1), the top three models were XGBOOST, random forest, and SVM, respectively. However, it was the XGBOOST, random forest, and logistic model for SSNs (104 benign *vs.* 104 malignant; 1:1). The performance of the established models on the validation dataset is summarized in *Table 2*, while that of the training dataset is shown in Table S5.

In addition, the ROC curves of the top three models in the training and validation datasets, as well as the performance of the best model in each fold on the validation dataset are shown in *Figure 4* (all nodules, *Figure 4A*,*B*,*C*; nodules ≤10 mm, *Figure 4D*,*E*,*F*) and *Figure 5* (solid nodules, *Figure 5A*,*B*,*C*; SSNs, *Figure 5D*,*E*,*F*). The

Table 1 Clinical characteristics of patients in the solid and subsolid group

Characteristics	Solid group			Subsolid group		
	Benign (n=306)	Malignant (n=242)	P value	Benign (n=104)	Malignant (n=519)	P value
Age, years	52±12	59±10	0.000	51±10	57±11	0.000
Sex, female	47.7	53.3	0.193	67.3	71.1	0.439
Smoking	35.0	38.8	0.350	21.2	16.2	0.218
History of malignancy	5.2	10.7	0.016	5.8	8.7	0.325
Family history of LC	4.9	7.9	0.155	8.7	10.6	0.551
Diameter, mm	13±4	14±4	0.000	9±3	12±4	0.000
Location, upper lobe	45.4	50.0	0.287	54.8	66.5	0.023
Shape, irregular	55.6	82.6	0.000	53.8	68.0	0.005
Spiculation	32.7	58.7	0.000	12.5	33.7	0.000
Lobulation	38.6	52.1	0.002	16.3	35.5	0.000
Red blood cell, 10^{12}/L	4.62±0.55	4.54±0.49	0.059	4.53±0.47	4.54±0.50	0.838
White blood cell, 10^{9}/L	5.75±1.60	6.12±2.01	0.015	5.87±1.65	5.79±1.75	0.702
Blood platelet, 10^{9}/L	176.68±56.73	177.11±56.96	0.930	172.81±53.63	177.12±57.96	0.484
NLR	2.06±1.24	2.34±1.70	0.023	2.27±1.49	2.17±1.43	0.518
PT, s	11.16±0.83	11.25±1.12	0.306	11.07±0.82	11.24±1.15	0.167
APTT, s	28.07±3.70	27.18±3.61	0.005	28.07±3.89	27.07±3.96	0.018
CEA, ng/mL	1.91±0.98	4.07±12.02	0.006	1.77±0.88	2.44±6.98	0.329
CYFRA21-1, ng/mL	1.96±0.73	2.04±0.87	0.242	1.85±0.60	2.09±1.05	0.001
NSE, ng/mL	12.78±4.46	13.26±4.24	0.200	12.71±4.06	14.57±5.14	0.001

Numeric variables were presented as mean ± standard deviation, category variables were presented in proportion. LC, lung cancer; NLR, neutrophil to lymphocyte ratio, PT, prothrombin time; APTT, activated partial thromboplastin time; CEA, carcinoembryonic antigen; CYFRA21-1, cytokeratin 19 fragment; NSE, neuron specific enolase.

performance of risk models for SSNs was quite weak (AUC in validation dataset, 0.65–0.76) and the XGBOOST model was even unstable (AUC, 1.00 in training *vs.* 0.65 in validation); therefore, the ROC curves of the random forest model are shown in *Figure 5F*.

Comparison of established clinical-radiomics models with Mayo model

The Mayo model was validated in all cases in each nodule group and was compared with the best corresponding clinical-radiomics model. *Table 3* summarizes the detailed predictive results. We found that the Mayo model, which was based on only six clinical characteristics, showed comparable discriminating ability with our clinical-radiomics model for SSNs (accuracy, 0.73 *vs.* 0.70; AUC, 0.75 *vs.* 0.73). However, it was inferior to the clinical-radiomics models for the other three nodule groups (accuracy, 0.55–0.67 *vs.* 0.80–0.86; AUC, 0.59–0.70 *vs.* 0.89–0.91).

Discussion

Accurate evaluation of the malignancy of pulmonary nodules plays an important role in lung cancer management. Moreover, solid nodules and SSNs exhibit different clinical courses, and guidelines for the management of pulmonary nodules have provided separate recommendations for the two types of nodules (9). Therefore, the current study based on clinical and radiomics features has established four models for all nodules (5–20 mm), nodules ≤10 mm, solid nodules, and SSNs.

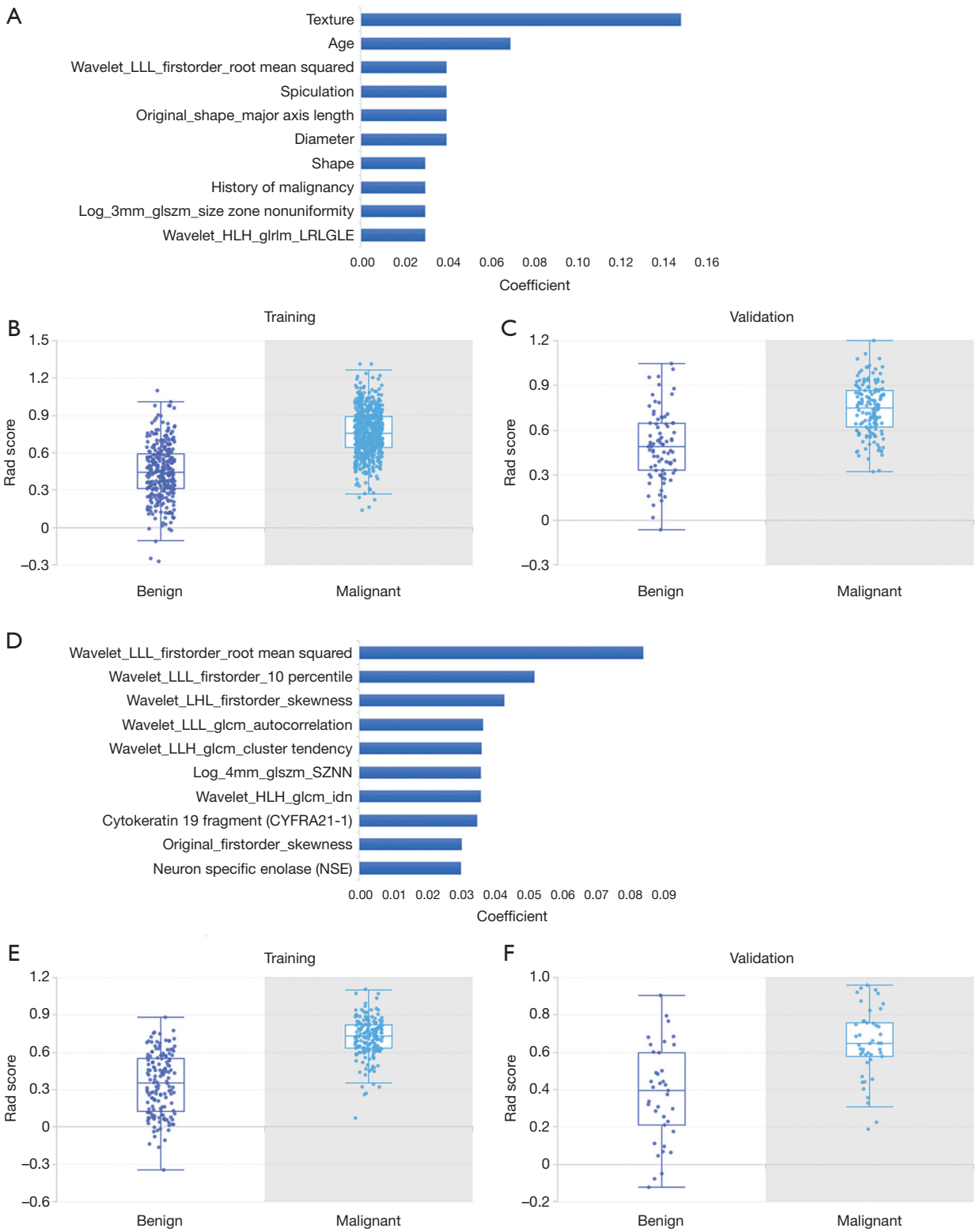

Figure 2 Feature selection based on LASSO analysis for all nodules (A,B,C) and the nodules less than 10 mm (D,E,F). A,D, top ten predictors sorted by absolute value of coefficients; B,C,E,F, rad-score boxplots of all selected features. LRLGLE, long run low gray level emphasis; SZNN, size zone nonuniformity normalized.

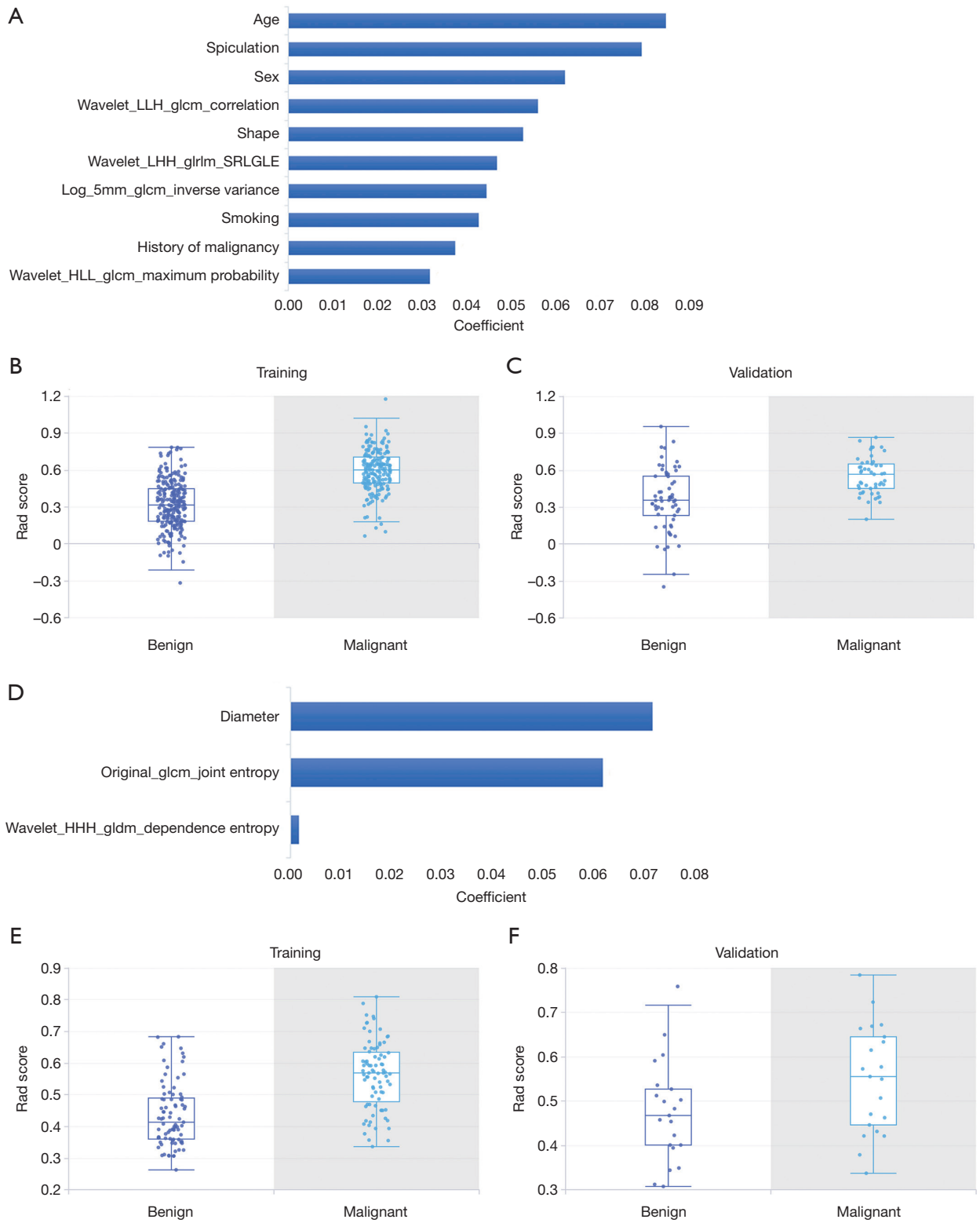

Figure 3 Feature selection based on LASSO analysis for solid nodules (A,B,C) and subsolid nodules (D,E,F). A, top ten predictors for solid nodules sorted by absolute value of coefficients; D, selected three predictors for subsolid nodules; B,C,E,F, rad-score boxplots of all selected features. SRLGLE, short run low gray level emphasis.

Table 2 Performance of established models on validation dataset

Group	Methods	Accuracy	F1 Score	Recall	Precision	Sensitivity	Specificity	AUC
All nodules	XGBOOST	0.86	0.89	0.93	0.87	0.93	0.73	0.91
	Random Forest	0.83	0.88	0.96	0.81	0.96	0.59	0.89
	SVM	0.77	0.83	0.88	0.79	0.88	0.55	0.81
Nodules≤10 mm	XGBOOST	0.82	0.84	0.86	0.82	0.86	0.76	0.90
	Random Forest	0.81	0.84	0.88	0.81	0.88	0.74	0.90
	SVM	0.74	0.78	0.83	0.74	0.83	0.64	0.80
Solid nodules	XGBOOST	0.80	0.78	0.78	0.77	0.78	0.82	0.89
	Random Forest	0.79	0.76	0.73	0.79	0.73	0.85	0.88
	SVM	0.71	0.66	0.65	0.68	0.65	0.75	0.77
Subsolid nodules	XGBOOST	0.62	0.63	0.64	0.62	0.64	0.60	0.65
	Random Forest	0.70	0.71	0.73	0.70	0.73	0.67	0.73
	Logistic	0.73	0.71	0.69	0.77	0.69	0.76	0.76

AUC, area under the ROC curve.

We previously established lung cancer risk models solely based on the clinical features of solid nodules and SSNs of different sizes (15). The clinical models showed an AUC of 0.70 and 0.71 for SSNs and solid nodules <15 mm, 0.72 and 0.81 for SSNs and solid nodules between 15 and 30 mm, respectively (15). It was obvious that the current models combining clinical and radiomics features exhibited greater discrimination ability, especially for nodules ≤10 mm (highest AUC, 0.90) and solid nodules (highest AUC, 0.89), while there was only a slight improvement for SSNs (highest AUC, 0.76). Similarly, when compared to the Mayo model (six predictors: age, smoking, history of cancer, diameter, spiculation, and upper lobe location), the established models demonstrated absolute superiority for all nodules, nodules ≤10 mm, and solid nodules, whereas the diagnostic advantages for SSNs were not obvious. The possible reason was that there were only a small number of benign SSNs available, and for data balance, the same number of malignant cases were matched. Therefore, due to the small sample size (208), trained SSN models can be unstable, of which only three risk predictors were selected.

An increasing number of SSNs have been encountered in routine clinical practice. Most early stage lung adenocarcinomas can manifest as SSNs with different degrees of invasion (16). Consequently, previous radiomics studies for SSNs focused more on identifying the invasiveness of lung adenocarcinomas (16-18). However, Gong *et al*. studied 182 histopathology-confirmed SSNs using radiomics analysis for nodule diagnosis [59 benign nodules, 50 adenocarcinoma in situ (AIS), 32 minimally invasive adenocarcinoma (MIA), and 41 invasive adenocarcinoma] (19). Their results showed an average AUC of 0.75 in distinguishing benign and malignant SSNs, which was consistent with the current study (AUC, 0.65–0.76). Moreover, their models also demonstrated poor performance in benign and AIS nodules (AUC, 0.55), and benign and MIA nodules (0.77), respectively (19). Nevertheless, a high AUC of 0.93, was observed for benign nodules and invasive adenocarcinomas (19). Hence, radiomics features have shown potential in predicting the malignancy of SSNs, but sufficient data is a priority to train a good model.

We noticed that the clinical characteristics could be as important as radiomics features in lung cancer risk prediction for solid nodules. Sixty percent of the top ten selected features were clinical variables, which have been identified in previous studies (7,20-22). The clinical variables were age, spiculation, sex, shape, smoking, and history of malignancy. When predicting malignancy of solid nodules, the clinical-based models exhibited an AUC of 0.81 to 0.89 (7,20-22), and one study pointed out that a VDT of 25–400 days was highly suggestive of malignancy (7). On the other hand, quantitative radiomics models have also demonstrated potential for diagnosing solid nodules, especially radiomics models created from gross tumor volume instead of peritumoral volumes (23). Therefore, the

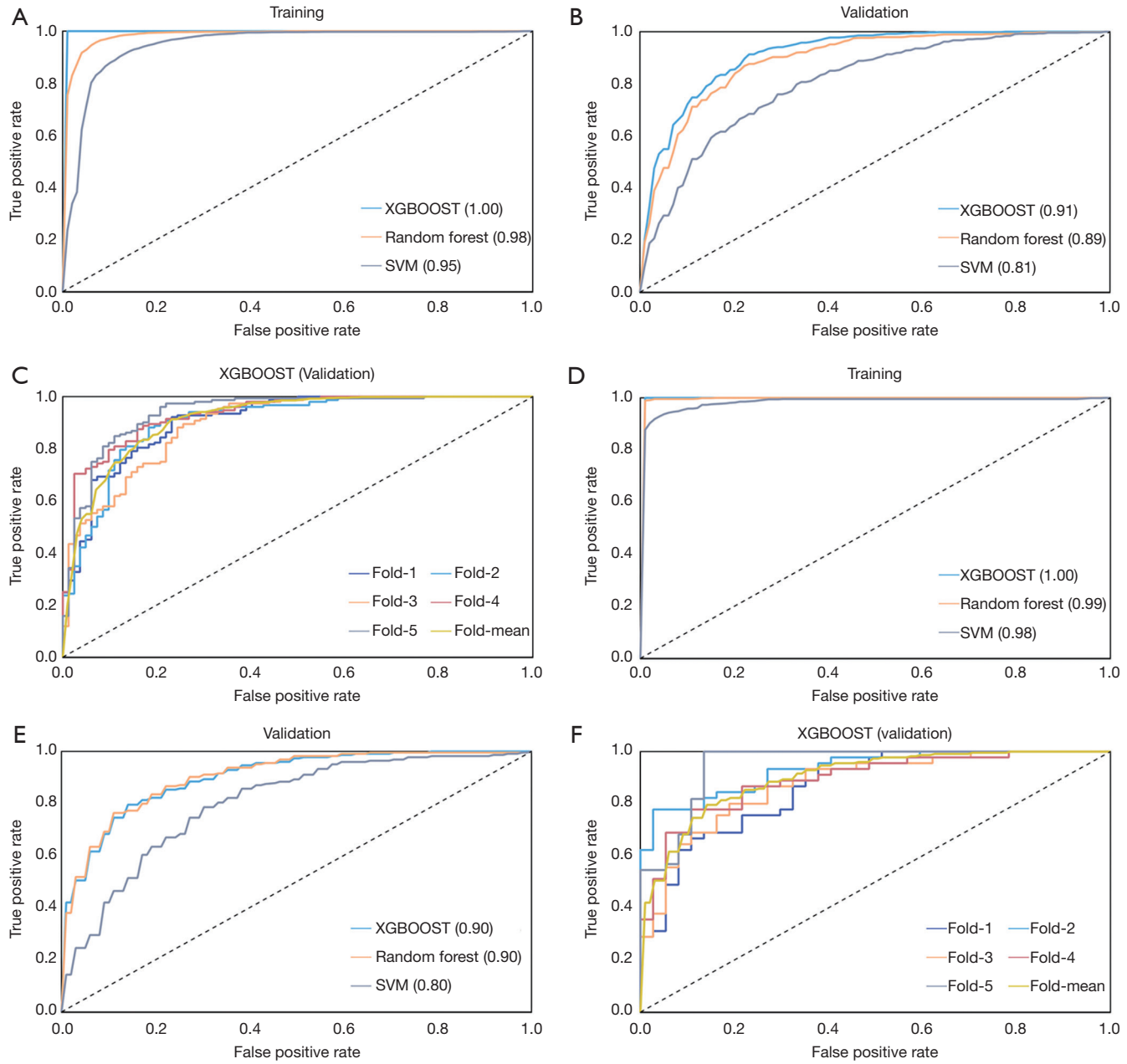

Figure 4 Receiver operating characteristic curves of established models for all nodules (A,B,C) and the nodules less than 10 mm (D,E,F). A,B,D,E, performance of top three models; C,F, performance of the XGBOOST model in each fold.

combination of clinical and quantitative radiomics features improved the performance of the clinical models developed in our previous study (15).

The Brock model, which is based on two screening cohorts (PanCan and BCCA; rates of cancer, 5.5% and 3.7%, respectively) demonstrated good discrimination and calibration for nodules ≤10 mm, with an AUC of 0.89 to 0.94 (8). Predictors of cancer in the model were all clinical variables, including older age, female sex, family history of lung cancer, emphysema, larger nodule size, upper lobe location, part-solid nodule type, lower nodule count, and spiculation (8). Regarding incidental pulmonary nodules ≤10 mm, Xu *et al.* predicted the malignancy of 127 sub-centimeter nodules using radiomics features and achieved

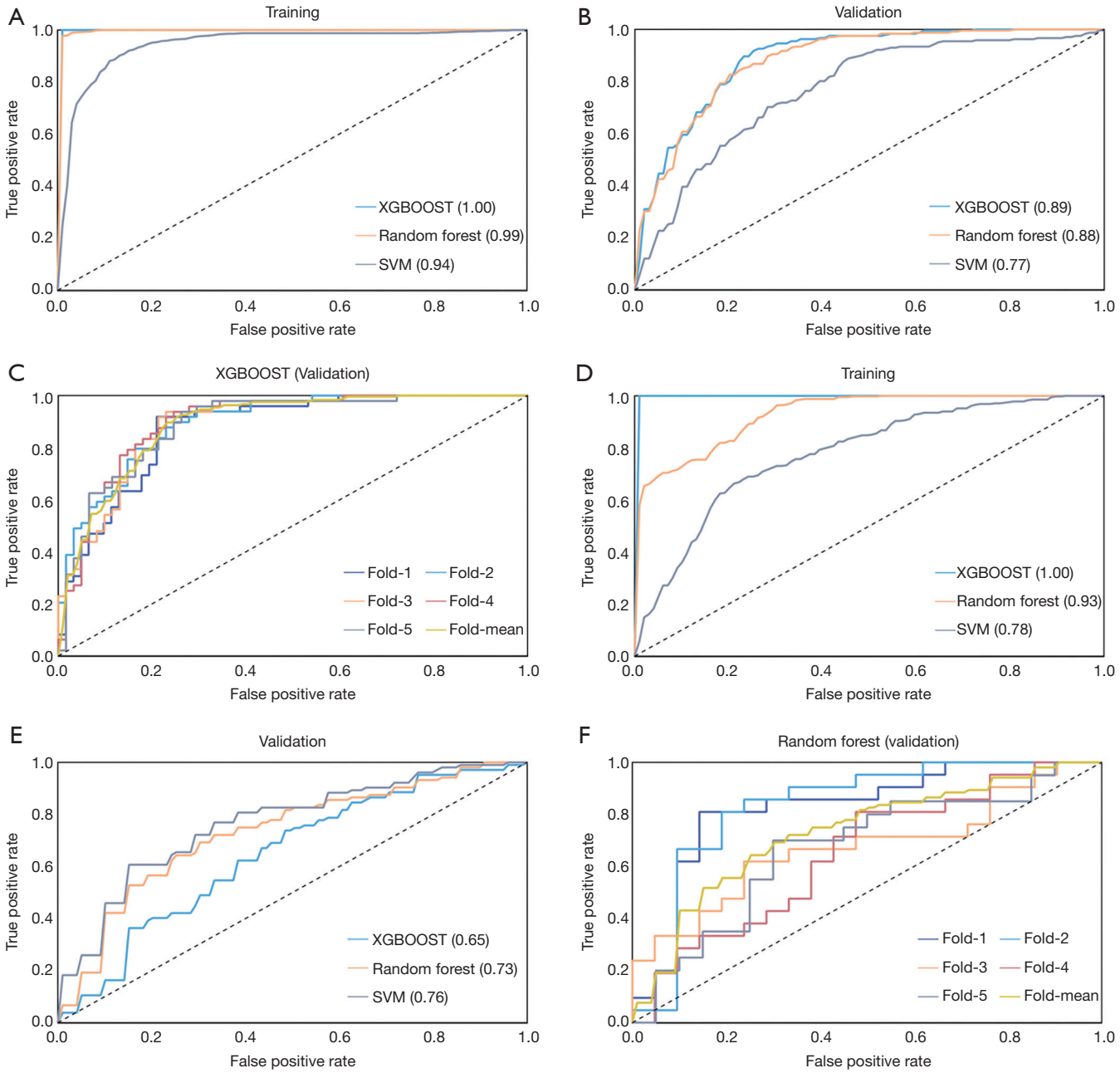

Figure 5 Receiver operating characteristic curves of established models for solid nodules (A,B,C) and subsolid nodules (D,E,F). A,B,D,E, performance of top three models; C, performance of the XGBOOST model in each fold for solid nodules; F, performance of the Random Forest model in each fold for subsolid nodules.

an AUC of 0.84 (24). However, in the current study of incidental pulmonary nodules, 67 clinical and radiomics features were selected for nodules ≤10 mm, and the risk models showed the highest AUC of 0.90. It is worth noting that radiomics features played a more important role in lung cancer risk prediction for incidental nodules ≤10 mm, with a high proportion of 80% among the top ten features, which were completely different from the other three nodule groups. Hence, radiomics features are meaningful in malignancy prediction for nodules ≤10 mm in routine

Table 3 The comparison between established clinical-radiomics model and Mayo model

Group	Model	Accuracy	Sensitivity	Specificity	AUC
All nodules (n=1,171)	XGBOOST	0.86	0.93	0.73	0.91
	Mayo	0.62	0.65	0.58	0.64
Nodules ≤10 mm (n=409)	XGBOOST	0.82	0.86	0.76	0.90
	Mayo	0.55	0.47	0.68	0.59
Solid nodules (n=548)	XGBOOST	0.80	0.78	0.82	0.89
	Mayo	0.67	0.60	0.74	0.70
Subsolid nodules (n=208)	Random Forest	0.70	0.73	0.67	0.73
	Mayo	0.73	0.72	0.76	0.75

The performance of established clinical-radiomics models were of validation dataset. AUC, area under the ROC curve.

clinical practice.

This study had some general and study-specific limitations. First, the study was carried out in a single medical center, in which bias could exist. In addition, this was a retrospective case-control study, which resulted in different scanner machines and non-uniform imaging protocols across patients. The difference should have a relevant impact on radiomics feature stability and thus prevented the establishment of robust risk models. Second, the growth rate of pulmonary nodules is one of the key characteristics associated with lung cancer probability, but we failed to apply the relevant parameters to build risk models in the current study. Usually, at least two thoracic CT scans prior to treatment are needed to calculate the growth rate of a nodule, but most of the patients we studied did not meet the criteria. Third, only a small number of SSNs were available for modeling; therefore, the performance of the established SSN models was unstable. Increasing the sample size, especially for benign SSNs, is warranted in future research. Last but not the least, we performed five-fold cross validation to evaluate the performance of established risk models, whereas the external validation is necessary.

Conclusions

In conclusion, based on both clinical and radiomics features, the current study established risk models to predict the malignancy of 5–20 mm pulmonary nodules. The models were developed for four nodule groups, including all nodules, nodules ≤10 mm, solid nodules, and SSNs. All models demonstrated excellent discrimination ability except for those of SSNs. Further studies are warranted to develop robust SSN models.

Acknowledgments

Funding: This work was supported by the National Key Development Plan for Precision Medicine Research (2017YFC0910004), and Central Guide Place-Free Exploration Project, Sichuan Provincial Department of Science and Technology (2020ZYD005).

Footnote

Reporting Checklist: The authors have completed the TRIPOD reporting checklist. Available at https://dx.doi.org/10.21037/jtd-21-80

Data Sharing Statement: Available at https://dx.doi.org/10.21037/jtd-21-80

Peer Review File: Available at https://dx.doi.org/10.21037/jtd-21-80

Conflicts of Interest: All authors have completed the ICMJE uniform disclosure form (available at https://dx.doi.org/10.21037/jtd-21-80). The authors have no conflicts of interest to declare.

Ethical Statement: The authors are accountable for all aspects of the work in ensuring that questions related to the accuracy or integrity of any part of the work are appropriately investigated and resolved. The study was conducted in accordance with the Declaration of Helsinki

(as revised in 2013). The study was approved by the institutional review board of the West China Hospital of Sichuan University (No.59). Informed consent was waived as this was a retrospective study and the privacy and identity information of the subjects were guaranteed.

References

1. Bray F, Ferlay J, Soerjomataram I, et al. Global cancer statistics 2018: GLOBOCAN estimates of incidence and mortality worldwide for 36 cancers in 185 countries. CA Cancer J Clin 2018;68:394-424.
2. Bai C, Choi CM, Chu CM, et al. Evaluation of Pulmonary Nodules: Clinical Practice Consensus Guidelines for Asia. Chest 2016;150:877-93.
3. MacMahon H, Naidich DP, Goo JM, et al. Guidelines for Management of Incidental Pulmonary Nodules Detected on CT Images: From the Fleischner Society 2017. Radiology 2017;284:228-43.
4. Wu W, Pierce LA, Zhang Y, et al. Comparison of prediction models with radiological semantic features and radiomics in lung cancer diagnosis of the pulmonary nodules: a case-control study. Eur Radiol 2019;29:6100-8.
5. Swensen SJ, Silverstein MD, Ilstrup DM, et al. The probability of malignancy in solitary pulmonary nodules. Application to small radiologically indeterminate nodules. Arch Intern Med 1997;157:849-55.
6. Herder GJ, van Tinteren H, Golding RP, et al. Clinical prediction model to characterize pulmonary nodules: validation and added value of 18F-fluorodeoxyglucose positron emission tomography. Chest 2005;128:2490-6.
7. Soardi GA, Perandini S, Motton M, et al. Assessing probability of malignancy in solid solitary pulmonary nodules with a new Bayesian calculator: improving diagnostic accuracy by means of expanded and updated features. Eur Radiol 2015;25:155-62.
8. McWilliams A, Tammemagi MC, Mayo JR, et al. Probability of cancer in pulmonary nodules detected on first screening CT. N Engl J Med 2013;369:910-9.
9. Kim TJ, Kim CH, Lee HY, et al. Management of incidental pulmonary nodules: current strategies and future perspectives. Expert Rev Respir Med 2020;14:173-94.
10. van Riel SJ, Sanchez CI, Bankier AA, et al. Observer Variability for Classification of Pulmonary Nodules on Low-Dose CT Images and Its Effect on Nodule Management. Radiology 2015;277:863-71.
11. van't Westeinde SC, de Koning HJ, Xu DM, et al. How to deal with incidentally detected pulmonary nodules less than 10mm in size on CT in a healthy person. Lung Cancer 2008;60:151-9.
12. van Griethuysen JJM, Fedorov A, Parmar C, et al. Computational Radiomics System to Decode the Radiographic Phenotype. Cancer Res 2017;77:e104-7.
13. Liao Z, Mohan R, Court L, et al. Radiomics of pulmonary nodules and lung cancer. Sci Rep 2017;6:86-91.
14. Yushkevich PA, Piven J, Hazlett HC, et al. User-guided 3D active contour segmentation of anatomical structures: Significantly improved efficiency and reliability. Neuroimage 2006;31:1116-28.
15. Zhang R, Tian PW, Chen BJ, et al. Predicting Lung Cancer Risk of Incidental Solid and Subsolid Pulmonary Nodules in Different Sizes. Cancer Manag Res 2020;12:8057-66.
16. Fan L, Fang M, Li Z, et al. Radiomics signature: a biomarker for the preoperative discrimination of lung invasive adenocarcinoma manifesting as a ground-glass nodule. Eur Radiol 2019;29:889-97.
17. Wu G, Woodruff HC, Shen J, et al. Diagnosis of Invasive Lung Adenocarcinoma Based on Chest CT Radiomic Features of Part-Solid Pulmonary Nodules: A Multicenter Study (vol 297, 2020192431, 2020). Radiology 2020;297:E282.
18. Zhao W, Xu Y, Yang Z, et al. Development and validation of a radiomics nomogram for identifying invasiveness of pulmonary adenocarcinomas appearing as subcentimeter ground-glass opacity nodules. Eur J Radiol 2019;112:161-8.
19. Gong J, Liu J, Hao W, et al. Computer-aided diagnosis of ground-glass opacity pulmonary nodules using radiomic features analysis. Phys Med Biol 2019;64:135015.
20. Chen XB, Yan RY, Zhao K, et al. Nomogram For The Prediction Of Malignancy In Small (8–20 mm) Indeterminate Solid Solitary Pulmonary Nodules In Chinese Populations. Cancer Manag Res 2019;11:9439-48.
21. Guo HY, Lin JT, Huang HH, et al. Development and Validation of a 18F-FDG PET/CT-Based Clinical Prediction Model for Estimating Malignancy in Solid

Pulmonary Nodules Based on a Population With High Prevalence of Malignancy. Clin Lung Cancer 2020;21:47-55.
22. She Y, Zhao L, Dai C, et al. Development and validation of a nomogram to estimate the pretest probability of cancer in Chinese patients with solid solitary pulmonary nodules: A multi-institutional study. J Surg Oncol 2017;116:756-62.
23. Wu S, Zhang N, Wu Z, et al. Can Peritumoral Radiomics Improve the Prediction of Malignancy of Solid Pulmonary Nodule Smaller Than 2 cm? Acad Radiol 2020. [Epub ahead of print]. doi: 10.1016/j.acra.2020.10.029.
24. Xu Y, Lu L, E LN, et al. Application of Radiomics in Predicting the Malignancy of Pulmonary Nodules in Different Sizes. AJR Am J Roentgenol 2019;213:1213-20.

Cite this article as: Zhang R, Sun H, Chen B, Xu R, Li W. Developing of risk models for small solid and subsolid pulmonary nodules based on clinical and quantitative radiomics features. J Thorac Dis 2021;13(7):4156-4168. doi: 10.21037/jtd-21-80

Supplementary

Table S1 Extracted radiomics features

First order (N=18)	Shape (N=14)	GLDM (N=14)	GLRLM (N=16)	GLSZM (N=16)	GLCM (N=22)
Interquartile Range	Voxel Volume	Gray Level Variance	Short Run Low Gray Level Emphasis	Gray Level Variance	Joint Average
Skewness	Maximum 3D Diameter	High Gray Level Emphasis	Gray Level Variance	Zone Variance	Joint Entropy
Uniformity	Mesh Volume	Dependence Entropy	Low Gray Level Run Emphasis	Gray Level Non-Uniformity Normalized	Cluster Shade
Median	Major Axis Length	Dependence Non-Uniformity	Gray Level Non-Uniformity Normalized	Size Zone Non-Uniformity Normalized	Maximum Probability
Energy	Sphericity	Gray Level Non-Uniformity	Run Variance	Size Zone Non-Uniformity	Idmn
Robust Mean Absolute Deviation	Least Axis Length	Small Dependence Emphasis	Gray Level Non-Uniformity	Gray Level Non-Uniformity	Joint Energy
Mean Absolute Deviation	Elongation	Small Dependence High Gray Level Emphasis	Long Run Emphasis	Large Area Emphasis	Contrast
Total Energy	Surface Volume Ratio	Dependence Non-Uniformity Normalized	Short Run High Gray Level Emphasis	Small Area High Gray Level Emphasis	Difference Entropy
Maximum	Maximum 2D Diameter Slice	Large Dependence Emphasis	Run Length Non-Uniformity	Zone Percentage	Inverse Variance
Root Mean Squared	Flatness	Large Dependence Low Gray Level Emphasis	Short Run Emphasis	Large Area Low Gray Level Emphasis	Difference Variance
90 Percentile	Surface Area	Dependence Variance	Long Run High Gray Level Emphasis	Large Area High Gray Level Emphasis	Idn
Minimum	Minor Axis Length	Large Dependence High Gray Level Emphasis	Run Percentage	High Gray Level Zone Emphasis	Idm
Entropy	Maximum 2D Diameter Column	Small Dependence Low Gray Level Emphasis	Long Run Low Gray Level Emphasis	Small Area Emphasis	Correlation
Range	Maximum 2D Diameter Row	Low Gray Level Emphasis	Run Entropy	Low Gray Level Zone Emphasis	Autocorrelation
Variance			High Gray Level Run Emphasis	Zone Entropy	Sum Entropy
10 Percentile			Run Length Non-Uniformity Normalized	Small Area Low Gray Level Emphasis	Sum Squares
Kurtosis					Cluster Prominence
Mean					Imc2
					Imc1
					Difference Average
					Id
					Cluster Tendency

https://dx.doi.org/10.21037/jtd-21-80

Table S2 Histopathological diagnosis of enrolled nodules

Pathological diagnosis	All nodules (N=1171)	Solid nodules (N=548)	Subsolid nodules (N=623)
Malignant nodules			
Adenocarcinomas	741 (97.37)	223 (92.15)	518 (99.81)
Squamous carcinomas	15 (1.97)	14 (5.78)	1 (0.19)
Other types	5 (0.66)	5 (2.07)	0 (0.00)
In total	761 (100.00)	242 (100.00)	519 (100.00)
Benign nodules			
Inflammatory nodules	255 (62.20)	182 (59.48)	73 (70.19)
Benign tumors	82 (20.00)	80 (26.14)	2 (1.92)
Other types	73 (17.80)	44 (14.38)	29 (27.89)
In total	410 (100.00)	306 (100.00)	104 (100.00)

Table S3 Details of missing data for CEA, CYFRA21-1 and NSE

	CEA	CYFRA21-1	NSE
Malignant nodules (N=761)			
Effective cases	562	537	513
Missing cases	199	224	248
Percentage of missing	0.26	0.29	0.33
Median, ng/ml	1.80	1.87	13.27
Benign nodules (n=410)			
Effective cases	241	228	227
Missing cases	169	182	183
Percentage of missing	0.41	0.44	0.45
Median, ng/ml	1.71	1.86	12.06

CEA, carcinoembryonic antigen; CYFRA21-1, cytokeratin 19 fragment; NSE, neuron specific enolase.

https://dx.doi.org/10.21037/jtd-21-80

Table S4 Selected features for all nodules, nodules ≤10 mm, solid and subsolid nodules.

Feature	Coefficient	Count
All nodules (features, n=74)		
texture	−0.1523835	1
age	0.06533589	2
wavelet_lll_firstorder_root mean squared	−0.04389031	3
spiculation	0.042131495	4
original_shape_major axis length	−0.040900707	5
diameter	0.036909364	6
shape	0.033710454	7
history of malignancy	0.03174518	8
log_3mm_glszm_size zone nonuniformity	0.0308566	9
wavelet_hh_glrlm_long run low gray level emphasis	0.030578818	10
wavelet_hl_glcm_maximum probability	−0.030241398	11
wavelet_lhh_glcm_idmn	0.027672501	12
sex	0.024286829	13
log_2mm_glcm_cluster prominence	−0.023833996	14
wavelet_hlh_glcm_idmn	−0.023355792	15
wavelet_llh_glcm_correlation	−0.022032931	16
family history of lung cancer	0.02008666	17
wavelet_hhh_firstorder_median	0.0199771	18
location	0.019024547	19
neuron specific enolase (NSE)	0.017194185	20
carcinoembryonic antigen (CEA)	0.0162424	21
aprothrombin time	−0.016034134	22
log_3mm_glszm_small area emphasis	0.015090621	23
wavelet_hh_glcm_inverse variance	−0.01478048	24
wavelet_hlh_glcm_cluster prominence	−0.013684566	25
wavelet_hhh_firstorder_skewness	−0.013468539	26
log_4mm_gldm_small dependence high gray level emphasis	0.013222083	27
original_gldm_small dependence low gray level emphasis	0.011755479	28
log_1mm_firstorder_robust mean absolute deviation	−0.01169028	29
wavelet_hhh_glrlm_short run low gray level emphasis	−0.011426748	30
wavelet_hhh_firstorder_median	−0.011410688	31
wavelet_hh_glszm_large area high gray level emphasis	0.01129744	32
wavelet_lll_glcm_correlation	0.011281525	33
wavelet_llh_gldm_small dependence low gray level emphasis	−0.011063043	34
wavelet_hll_firstorder_skewness	−0.010512063	35
blood platelet	0.009993129	36
wavelet_lll_firstorder_skewness	0.009779177	37
wavelet_hlh_firstorder_skewness	0.009215213	38
log_4mm_glszm_size zone nonuniformity normalized	−0.008668284	39
wavelet_lhh_firstorder_mean	0.008643762	40
log_5mm_gldm_large dependence high gray level emphasis	0.008336597	41
log_3mm_glcm_imc1	0.008259805	42
wavelet_lhh_glszm_small area low gray level emphasis	−0.008223074	43
log_5mm_glszm_gray level variance	0.00729779	44
log_1mm_gldm_dependence nonuniformity normalized	−0.006937272	45
log_4mm_glszm_small area low gray level emphasis	0.00678647	46
log_5mm_glcm_idn	0.006554504	47
prothrombin time	0.006366947	48
log_5mm_glszm_size zone nonuniformity	0.00632784	49
wavelet_llh_glcm_cluster tendency	−0.005792676	50
wavelet_hhh_gldm_small dependence low gray level emphasis	−0.005367769	51
wavelet_hl_glszm_large area high gray level emphasis	−0.005241822	52
log_3mm_gldm_large dependence low gray level emphasis	−0.004694483	53
log_3mm_gldm_small dependence low gray level emphasis	−0.004678963	54
wavelet_hhl_glcm_correlation	−0.004455136	55
wavelet_hhh_glcm_joint average	0.004391401	56
log_2mm_glszm_low gray level zone emphasis	−0.004090064	57
log_2mm_glcm_cluster shade	0.003850946	58
wavelet-ll_firstorder_10 percentile	−0.003925614	59
original_firstorder_kurtosis	0.003857596	60
wavelet_hlh_glcm_correlation	−0.003388095	61
log_5mm_glcm_difference variance	0.002327749	62
wavelet_lhh_glcm_cluster shade	−0.002186119	63
log_2mm_glszm_large area emphasis	0.002185869	64
wavelet_lhl_firstorder_median	−0.001794971	65
log_1mm_glszm_large area low gray level emphasis	0.001774499	66
log_2mm_glszm_small area low gray level emphasis	−0.000730023	67
lobulation	0.000719328	68
wavelet_hhh_firstorder_mean	−0.000579703	69
log_5mm_glszm_large area low gray level emphasis	0.000499966	70
log_5mm_glszm_zone percentage	0.00046101	71
log_5mm_firstorder_kurtosis	0.000458805	72
log_5mm_firstorder_maximum	0.000431416	73
log_3mm_glszm_small area low gray level emphasis	−0.000344796	74
nodules≤ 10 mm (features, n=67)		
wavelet_lll_firstorder_root mean squared	−0.085387975	1
wavelet_lll_firstorder_10 percentile	−0.052760538	2
wavelet_lhl_firstorder_skewness	0.04368638	3
wavelet_lll_glcm_autocorrelation	−0.037189778	4
wavelet_llh_glcm_cluster tendency	−0.036917366	5
log_4mm_glszm_size zone nonuniformity normalized	−0.03664406	6
wavelet_hlh_glcm_idn	−0.03649864	7
cytokeratin 19 fragment (cyfra21_1)	0.03539686	8
original_firstorder_skewness	0.030780079	9
neuron specific enolase (NSE)	0.03052495	10
wavelet_llh_glcm_correlation	−0.029156856	11
log_5mm_glszm_large area low gray level emphasis	0.028894316	12
texture	−0.028710542	13
diameter	0.027427517	14
spiculation	0.027001955	15
wavelet_hl_gldm_dependence variance	0.025864117	16
log_4mm_glszm_small area low gray level emphasis	0.025831908	17
wavelet_lhl_firstorder_kurtosis	−0.024995528	18
lobulation	0.02439137	19
log_1mm_glcm_idmn	0.024272965	20
carcinoembryonic antigen (CEA)	0.024164213	21
wavelet_hhl_firstorder_mean	0.023521949	22
wavelet_lll_glcm_idmn	0.023353273	23
history of malignancy	0.021469418	24
wavelet_hll_glcm_idmn	−0.01970135	25
wavelet_lhh_firstorder_median	0.019359384	26
wavelet_hlh_glcm_correlation	−0.018328678	27
log_1mm_gldm_large dependence low gray level emphasis	−0.018173037	28
wavelet_hhl_firstorder_skewness	−0.016232854	29
wavelet_hhh_firstorder_median	−0.015945809	30
wavelet_hlh_glcm_cluster shade	0.015767435	31
log_2mm_firstorder_kurtosis	−0.014968184	32
wavelet_llh_firstorder_skewness	0.014899718	33
wavelet_llh_gldm_large dependence low gray level emphasis	−0.013667205	34
log_5mm_glcm_idn	0.013578288	35
wavelet_llh_firstorder_skewness	−0.013431707	36
log_4mm_gldm_large dependence high gray level emphasis	0.012531875	37
log_3mm_glszm_low gray level zone emphasis	−0.012381748	38
log_5mm_glcm_cluster prominence	0.012375816	39
original_shape_maximum 2d diameter slice	−0.0119441	40
log_2mm_gldm_large dependence low gray level emphasis	0.011709616	41
prothrombin time	0.011531907	42
log_3mm_glcm_imc1	0.010953448	43
wavelet_hlh_glcm_autocorrelation	−0.010753098	44
wavelet_lhh_glszm_zone entropy	0.010242574	45
log_4mm_glcm_inverse variance	0.009940656	46
log_4mm_glcm_cluster prominence	0.009320633	47
wavelet_hh_gldm_large dependence high gray level emphasis	−0.009075509	48
wavelet_llh_firstorder_interquartile range	−0.008467706	49
age	0.007600686	50
red blood cell	−0.007256369	51
wavelet_hhl_glcm_correlation	−0.007253644	52
log_4mm_firstorder_kurtosis	0.007172	53
wavelet_hll_firstorder_skewness	−0.007003864	54
wavelet_hhh_gldm_large dependence high gray level emphasis	0.004918731	55
log_5mm_glszm_small area low gray level emphasis	−0.004511342	56
original_shape_elongation	−0.004177442	57
wavelet_llh_gldm_large dependence high gray level emphasis	0.003418303	58
log_3mm_glszm_large area high gray level emphasis	0.003353799	59
original_shape_flatness	−0.002683324	60
log_2mm_glszm_gray level variance	−0.002040724	61
log_1mm_glcm_correlation	0.001979248	62
wavelet_hl_glszm_large area low gray level emphasis	0.001149169	63
log_2mm_glszm_gray level nonuniformity	0.00089789	64
wavelet_lhh_glszm_gray level nonuniformity normalized	−0.000575396	65
log_3mm_firstorder_kurtosis	−0.000409742	66
original_glcm_cluster shade	6.95E−06	67
Solid nodules (features, n=51)		
age	0.08456472	1
spiculation	0.078593165	2
sex	0.061542835	3
wavelet_llh_glcm_correlation	−0.055488173	4
shape	0.052257538	5
wavelet_lhh_glrlm_short run low gray level emphasis	−0.04648701	6
log_5mm_glcm_inverse variance	−0.044164747	7
smoking	0.04239887	8
history of malignancy	0.037123434	9
wavelet_hll_glcm_maximum probability	−0.031502098	10
original_firstorder_10 percentile	−0.0312687	11
log_1mm_firstorder_interquartile range	−0.027092805	12
wavelet_hhl_firstorder_median	−0.027003296	13
wavelet_hhh_firstorder_median	0.024898052	14
carcinoembryonic antigen (CEA)	0.024303196	15
red blood cell	−0.021868614	16
original_shape_sphericity	0.021541847	17
aprothrombin time	−0.020654099	18
wavelet_hhh_glcm_cluster shade	−0.019607673	19
cytokeratin 19 fragment (cyfra21_1)	−0.018995605	20
wavelet_hhh_glcm_cluster prominence	−0.01898479	21
log_5mm_glszm_large area low gray level emphasis	−0.018560542	22
wavelet_hhh_glszm_large area emphasis	0.018066432	23
wavelet_llh_glszm_large area low gray level emphasis	0.01795587	24
wavelet_lll_firstorder_root mean squared	−0.017841883	25
log_1mm_glszm_large area low gray level emphasis	−0.01751925	26
wavelet_lhl_firstorder_median	−0.017030738	27
wavelet_llh_gldm_large dependence high gray level emphasis	−0.014039104	28
wavelet_lll_glcm_correlation	0.013814446	29
log_5mm_glszm_gray level nonuniformity normalized	−0.010168748	30
log_5mm_firstorder_maximum	0.010164706	31
original_gldm_ low gray level emphasis	0.009151111	32
original_shape_elongation	0.009042126	33
log_1mm_gldm_large dependence low gray level emphasis	−0.008320518	34
wavelet_hll_firstorder_skewness	−0.008298235	35
log_3mm_glszm_gray level nonuniformity	0.008272954	36
log_1mm_firstorder_skewness	−0.007213732	37
neuron specific enolase (NSE)	0.007036805	38
wavelet_hhh_firstorder_skewness	0.006946954	39
log_2mm_glcm_maximum probability	−0.006592018	40
wavelet_hlh_glcm_cluster prominence	−0.005666115	41
log_5mm_glszm_gray level variance	0.005162543	42
log_3mm_firstorder_skewness	0.005006426	43
log_2mm_glszm_large area low gray level emphasis	−0.004775111	44
log_5mm_glszm_zone percentage	0.004358722	45
diameter	0.003045135	46
white blood cell	0.001779955	47
wavelet_lll_firstorder_uniformity	−0.000929418	48
log_4mm_gldm_small dependence high gray level emphasis	0.000884861	49
wavelet_hhh_firstorder_mean	0.000599027	50
wavelet_lhl_glcm_cluster prominence	0.000421362	51
Subsolid nodules (features, n=3)		
diameter	0.071469665	1
original_glcm_joint entropy	0.061700333	2
wavelet_HHH_gldm_dependence entropy	0.001622507	3

Table S5 Performance of established models on training dataset

Group	Methods	Accuracy	F1 Score	Recall	Precision	Sensitivity	Specificity	AUC
All nodules	XGBOOST	1.00	1.00	1.00	1.00	1.00	1.00	1.00
	Random Forest	0.92	0.94	0.99	0.90	0.99	0.79	0.98
	SVM	0.90	0.92	0.97	0.88	0.97	0.76	0.95
Nodules ≤10 mm	XGBOOST	1.00	1.00	1.00	1.00	1.00	1.00	1.00
	Random Forest	0.98	0.98	1.00	0.97	1.00	0.97	0.99
	SVM	0.93	0.94	0.97	0.91	0.97	0.88	0.98
Solid nodules	XGBOOST	1.00	1.00	1.00	1.00	1.00	1.00	1.00
	Random Forest	0.98	0.98	0.99	0.98	0.99	0.98	0.99
	SVM	0.88	0.87	0.90	0.85	0.90	0.87	0.94
Subsolid nodules	XGBOOST	1.00	1.00	1.00	1.00	1.00	1.00	1.00
	Random Forest	0.80	0.81	0.83	0.79	0.83	0.78	0.93
	Logistic	0.73	0.72	0.70	0.74	0.70	0.76	0.78

AUC, area under the ROC curve.

https://dx.doi.org/10.21037/jtd-21-80